

1 **SARS-CoV-2 D614G Variant Exhibits Enhanced Replication *ex vivo* and Earlier
2 Transmission *in vivo***

3 Yixuan J. Hou^{1§}, Shihō Chiba^{4§}, Peter Halfmann⁴, Camille Ehre⁵, Makoto Kuroda⁴, Kenneth H
4 Dinnon III², Sarah R. Leist¹, Alexandra Schäfer¹, Noriko Nakajima⁶, Kenta Takahashi⁶, Rhianna
5 E. Lee⁵, Teresa M. Mascenik⁵, Caitlin E. Edwards¹, Longping V. Tse¹, Richard C. Boucher⁵,
6 Scott H. Randell⁵, Tadaki Suzuki⁶, Lisa E. Gralinski¹, Yoshihiro Kawaoka^{3,4*} and Ralph S.
7 Baric^{1,2*}

8

9 ¹ Department of Epidemiology, University of North Carolina at Chapel Hill, Chapel Hill, NC, USA

10 ² Department of Microbiology and Immunology, University of North Carolina at Chapel Hill,
11 Chapel Hill, NC, USA

12 ³ Division of Virology, Department of Microbiology and Immunology, Institute of Medical Science,
13 University of Tokyo, Tokyo, Japan

14 ⁴ Influenza Research Institute, Department of Pathobiological Sciences, School of Veterinary
15 Medicine, University of Wisconsin, Madison, WI, USA

16 ⁵ Marsico Lung Institute, University of North Carolina at Chapel Hill, Chapel Hill, NC, USA

17 ⁶ Department of Pathology, National Institute of Infectious Diseases, Tokyo, Japan

18

19 [§] These authors contribute equally.

20 *Address correspondence to: Yoshihiro Kawaoka, yoshihiro.kawaoka@wisc.edu; Ralph S. Baric,
21 rbaric@email.unc.edu

22

23 **Abstract**

24 The D614G substitution in the S protein is most prevalent SARS-CoV-2 strain circulating
25 globally, but its effects in viral pathogenesis and transmission remain unclear. We engineered
26 SARS-CoV-2 variants harboring the D614G substitution with or without nanoluciferase. The
27 D614G variant replicates more efficiently in primary human proximal airway epithelial cells and
28 is more fit than wildtype (WT) virus in competition studies. With similar morphology to the WT
29 virion, the D614G virus is also more sensitive to SARS-CoV-2 neutralizing antibodies. Infection
30 of human ACE2 transgenic mice and Syrian hamsters with the WT or D614G viruses produced

31 similar titers in respiratory tissue and pulmonary disease. However, the D614G variant exhibited
32 significantly faster droplet transmission between hamsters than the WT virus, early after
33 infection. Our study demonstrated the SARS-CoV2 D614G substitution enhances infectivity,
34 replication fitness, and early transmission.

35

36 **Main text**

37 The ongoing pandemic of Coronavirus Disease 2019 (COVID-19), caused by Severe Acute
38 Respiratory Syndrome Coronavirus 2 (SARS-CoV-2), has resulted in an unprecedented impact
39 on human society. Since its emergence in December 2019, SARS-CoV-2 has rapidly spread
40 worldwide, causing > 26 million cases and >900 thousand deaths as of early September 2020.
41 Compared to SARS-CoV (2003 to 2004) and Middle East respiratory syndrome coronavirus
42 (MERS-CoV) infection (2012 to present), SARS-CoV-2 infection causes a broader spectrum of
43 acute and chronic disease manifestations and exhibits greater transmissibility. Many patients
44 develop asymptomatic or mild disease, but some SARS-CoV-2-infected individuals develop
45 severe lower respiratory infections that can progress to an acute respiratory distress syndrome
46 (ARDS), strokes, cardiac pathology, gastrointestinal disease, coagulopathy, and a
47 hyperinflammatory shock syndrome (1–3). Ciliated cells in the respiratory epithelium and type 2
48 pneumocyte in the alveoli are the major targets of SARS-CoV-2 (4). Viral entry is mediated by
49 the interaction between viral spike (S) glycoprotein and host receptor angiotensin-converting
50 enzyme 2 (ACE2). To date, enormous efforts have focused on developing vaccines and
51 therapeutic antibodies targeting the S protein using early ancestral isolates that have been
52 replaced by novel contemporary strains (5, 6).

53

54 Pandemic spread of a virus in naïve populations may select for mutations that may alter
55 pathogenesis, virulence and/or transmissibility. Despite the presence of a CoV proof-reading
56 function (7, 8), recent reports identified an emergent D614G substitution in the spike

57 glycoprotein of SARS-CoV-2 strains that is now the most prevalent form globally. Patients
58 infected with the D614G-bearing SARS-CoV-2 are associated with higher viral loads in the
59 upper respiratory tract, but not altered disease severity (5, 9). SARS-CoV2 S pseudotyped
60 viruses encoding the D614G mutation were reported to exhibit increased infectivity in
61 continuous cells lines and increased sensitivity to neutralization (5, 10). Structural analyses also
62 revealed that the receptor binding domains (RBD) in the G614-form S protein occupy a higher
63 percentage in the open conformation than the D614-form, implying an improved ability to bind to
64 ACE2 receptor (11, 12). However, the D614G substitution has yet to be evaluated in the
65 authentic SARS-CoV-2 infection models, and its function in viral pathogenesis and
66 transmissibility remains unclear.

67
68 Previously, we generated a SARS-CoV-2 reverse genetics system based on the WA1 strain and
69 developed primary human airway epithelial cells, human ACE2 transgenic mice, and golden
70 Syrian hamsters as SARS-CoV-2 infection models (4, 13, 14). To address the function of the
71 D614G substitution in SARS-CoV-2 replication and transmissibility, we generated an isogenic
72 variant containing the D614G mutation in the S glycoprotein, along with a second variant that
73 contained the nanoLuciferease (nLuc) gene in place of the accessory gene 7a (Fig 1A). To
74 examine whether the D614G substitution enhanced authentic SARS-CoV-2 entry, four
75 susceptible cell lines were infected with wildtype (WT)-nLuc and D614G-nLuc viruses at an MOI
76 of 0.1. After a 1h incubation, cells were washed three times with PBS and cultured in medium
77 containing SARS-CoV-2 neutralizing antibodies to prevent viral spreading. Luciferase signals
78 representing initial entry events were measured at 8h post infection (Fig. 1B). In accord with
79 pseudovirus studies (5, 6), the D614G-nLuc infection resulted in a 0.5 to 2-fold higher transgene
80 expression as compared with WT-nLuc virus. Replication kinetics comparing WT and D614G
81 viruses were performed utilizing multi-step growth curves in cell lines (Fig 1C). Although the
82 D614G variant showed similar or slightly higher titers at the early time point (8h), its peak titers

83 were significantly lower than the WT virus in Vero-E6 and A549-ACE2 cell lines but not in Vero-
84 81 and Huh7. These data suggest that the D614G substitution may modestly enhances SARS-
85 CoV-2 entry and replication in some immortalized cell lines.

86

87 Primary human airway epithelial cells from different regions of the human respiratory tract
88 display different susceptibilities to SARS-CoV-2 infection, with the nasal epithelium being most
89 susceptible (4). To evaluate the replication of SARS-CoV-2 D614G variant in the human
90 respiratory tract, we compared WT and the D614G growth kinetics in primary human nasal
91 epithelial (HNE) from five donors, large (proximal) airway epithelial (LAE) from four donors, and
92 distal lung small airway epithelial (SAE) cells from three donors. Cultures from the same donor
93 were infected with either WT or D614G virus in triplicate (Fig. 1D to E, S1A to 1B). Both viruses
94 infect mainly ciliated cells in the primary pulmonary cultures (Fig. S1C). Paired t-test analysis
95 suggests the D614G-infected HNE at 24, 48 and 72h, and LAE cultures at 48h exhibited
96 significantly higher titers than cultures infected with the WT virus. This enhancement was not
97 observed in any timepoints in distal lung SAE cultures derived from three donors. To further
98 compare the replication fitness between the two variants in the human airway epithelia,
99 competitive co-infection assays were performed in LAE cultures infected simultaneously with
100 both viruses (Fig. 1G). After three continuous passages at 72h intervals, the D614G variant
101 became dominant in the cultures regardless of whether the WT virus was at a 1:1 or 10:1 ratio
102 over the isogenic D614G mutant (Fig. 1H and 1I). Taken together, these data suggest the
103 D614G substitution enhances SARS-CoV-2 replication fitness in the primary epithelial cells, with
104 a marked advantage in the upper respiratory tract epithelial cells in nasal and large (proximal)
105 airway epithelia.

106

107 Next, scanning and transmission electron microscopy (SEM and TEM) were performed to
108 visualize virions present on the surface of primary human airway cell cultures and did not detect

109 significant differences in virion morphology (Fig. 2A and B). The number of spike proteins on
110 projections of individual virions was also not significantly different between the two viruses (Fig.
111 2C). Further, differences in spike cleavage patterns were not observed between the two viruses
112 in western blot analysis (Fig. 2D), in contrast to observations reported from a pseudovirus study
113 (15). To compare antibody neutralization properties with reported pseudotyped virus assays
114 (10), neutralization activity was measured in 10 serum samples from D614 (WT) spike-
115 vaccinated mice using the nLuc-expressing recombinant SARS-CoV-2 encoding either WT or
116 D614G spike. The serum samples show 0.8 to 5.1-fold higher half-maximal inhibitory dilution
117 (ID_{50}) values against the D614G virus than the WT virus, suggesting the D614G substitution
118 rendered SARS-CoV-2 more sensitive to neutralizing antibodies (Fig. 2E and 2F). In addition,
119 six SARS-CoV-2 RBD-binding neutralizing antibodies were evaluated and exhibited no
120 significant difference in half-maximal inhibitory concentration (IC_{50}) values against both viruses.

121
122 To evaluate the function of the D614G substitution in viral pathogenesis, hACE2 transgenic
123 mice and Syrian hamsters were infected with equal plaque-forming units (PFU) of WT or D614G
124 viruses. Previously, we showed that SARS-CoV-2 infection in hACE2 mice exhibited a mild
125 disease phenotype, characterized by high viral titers in the lung but minimum weight loss and
126 undetectable nasal titers (14). Two groups of hACE2 mice infected with WT and D614G viruses
127 exhibited undetectable viral titers in nasal turbinates and similar lung viral titers at day 2 and 5
128 post infection. One mouse (1/5) from both groups exhibited detectable viral titers in the brain (Fig.
129 3A). With respect to hamster studies, lung and nasal turbinate tissues collected at day 3 and 6
130 pi exhibited similar viral titers in each group (Fig. 3B and 3C). However, the D614G-infected
131 hamsters lost modestly more body weight than those infected with the WT virus (Fig. 3D).
132 Immunohistochemistry (IHC) shows similar levels of SARS-CoV-2 nucleocapsid protein in the
133 hamster lung tissue collected at day 3, 6 and 9 from both groups (Fig. 3E, 3 G-i).
134 Histopathological examination revealed similar severe pulmonary lesion with inflammatory cell

135 infiltration in the alveolar walls and air spaces, pulmonary edema, and alveolar hemorrhage in
136 both of the hamsters on day 3, extended across larger areas on day 6, and then exhibiting
137 partial resolution by day 9 (Fig. 3F). Notably, there was no significant difference in the size of
138 the lung lesions (Fig. 3G-ii) and the histological severity (Fig. 3G-iii). Taking together, the
139 D614G substitution marginally enhances SARS-CoV-2 pathogenesis in the hamster, but not
140 mouse models.

141
142 To evaluate the role of the D614G substitution in SARS-CoV-2 respiratory droplet
143 transmissibility, we set up eight pairs of hamsters for each virus as described previously (16).
144 Each pair comprised a naïve hamster adjacent to an infected animal 1 day after infection (Fig.
145 S2). Viral titers in the nasal wash samples from both infected and exposed animals were
146 measured. Both WT and D614G were transmitted efficiently to naive hamsters evident by
147 positive nasal wash samples detected in all exposed animals at day 4 (Fig. 3H). The infected
148 groups at all three timepoints and the exposure groups at 4 and 6 dpi exhibit similar viral titers
149 between WT and D614G viruses. However, five of eight hamsters exposed to the D614G-
150 infected group showed infection and detectable viral shedding at day 2 while those exposed to
151 the WT-infected group had no infection and viral shedding ($p = 0.0256$, Fisher exact test).
152 These data suggest the D614G variant transmits significantly faster than the WT virus through
153 droplets and aerosols between hamsters.

154
155 Emerging viruses, like Sarbecoviruses, Alphaviruses, and Filoviruses, have undergone
156 sequential rounds of evolution while adapting to the new human hosts in epidemic or pandemic
157 settings (17–19). Among Sarbecoviruses, mutations in the Spike glycoprotein have been
158 associated with altered pathogenesis, receptor usage, and neutralization (20–22), potentially
159 challenging the development of vaccine and therapeutic antibodies that are urgently needed at
160 present. The emergent D614G mutation in the spike glycoprotein of SARS-CoV-2 strains has

161 raised significant concerns about potential enhancements in transmissibility, antigenicity and/or
162 pathogenesis. Using authentic live recombinant viruses, the infectivity and fitness of D614G
163 isogenic virus were compared in primary human cells and its pathogenesis and transmissibility
164 were tested in hamsters and hACE2 mice. Our data unilaterally support a critical role for the
165 D614G mutation in enhanced virus infectivity, growth and fitness in human nasal and proximal
166 airway epithelia, but not in the lower respiratory tract airway epithelium from multiple donors.
167 These *ex vivo* human airway culture data are consistent with the moderately increased
168 pathogenicity, as shown by body weight changes, and improved transmission of the D614G
169 variant in the hamster models of human disease.

170

171 Using pseudotype viruses, the D614G mutation has been suggested to increase proteolytic
172 cleavage and S glycoprotein incorporation into virions, reduce S1 loss and promote enhanced
173 infectivity *in vitro* (5, 6, 15). Our Western blot and SEM studies demonstrated no obvious
174 differences in proteolytic processing or S incorporation into isogenic virions encoding the D614G
175 mutations, perhaps reflecting differences in S trimer incorporation and presentation between
176 authentic and pseudotyped viruses. However, our data are consistent with recent studies
177 indicate that D614G alters spike trimer hydrogen-bond interactions, reorienting the RBD into an
178 “up” conformation, increasing ACE2 receptor binding and infectivity (11, 12). Our data
179 demonstrate that SARS-CoV2 D614G recombinant viruses are significantly more infectious in
180 some continuous cells in culture, but more importantly, in multiple patient codes of nasal and
181 large airway epithelial cells derived from the upper respiratory, but not lower respiratory tract.
182 Direct competition experiments also demonstrate that the SARS-CoV2 D614G isogenic virus
183 displays a significant advantage following passage in primary human large airway epithelial cells
184 *in vitro*. Together, these data strongly support the role of the nasal epithelium and the D614G
185 mutation in enhanced infectivity and transmission in human populations (9). These findings are

186 consistent with the preferential transmission of throat SARS-CoV-2 microvariants, over sputum
187 microvariants in human transmission chains and in influenza virus infected ferrets (23).

188

189 Patients infected with the D614G variant could not be conclusively linked to increased disease
190 severity in humans (5, 9). The hACE2 transgenic mouse study demonstrated equivalent virus
191 titers in the lungs and nasal turbinates. In contrast, the isogenic D614G recombinant virus
192 infection of hamsters resulted in significant differences in weight loss, but not pathology or virus
193 replication in the lung and nasal turbinates. In transmission studies, the D614G isogenic was
194 transmitted significantly faster to adjacent animals early in infection, demonstrating that the
195 substitution preserved efficient transmission phenotypes *in vivo*. As SARS-CoV2 replicates
196 preferentially in the nasal and olfactory epithelium, characterized by subtle differences driven by
197 differences in ACE2 and TMPRSS2 cell type specific expression patterns across species (4, 24,
198 25), all of these data are consistent with a model of increased replication in the nasal epithelium
199 and large airway epithelium, leading to enhanced virus growth and earlier transmissibility.

200

201 The effect of the D614G variant on vaccine efficacy has been of major concern. Consistent with
202 previous studies (10), we demonstrated the increased sensitivity of the SARS-CoV2 D614G-
203 nLuc variant to the antisera from D-form spike (WT) vaccinated mice. Similar findings have been
204 reported using sera from ChAd-vaccinated mice (26). Together with similar neutralization
205 properties against six SARS-CoV-2 mAbs, these data suggest that the current vaccine and mAb
206 approaches directed against WT spike should be effective against the D614G strains. In
207 addition, these data support the hypothesis that early in the pandemic S-trimer reorganization
208 favors transmission over-sensitivity to neutralization, a phenotype that might be expected to
209 emerge as a new virus spreads through a large naive population and then undergoes new
210 evolutionary change as herd immunity increase with time.

211

212 In summary, our data support the critical need to periodically review SARS-CoV-2 contemporary
213 isolates across the globe and identify the emergence of new variants with increased
214 transmission and pathogenesis and/or altered antigenicity, especially as levels of human herd
215 immunity and interventions alter the selective forces that operate on the genome. Our data
216 suggest that vaccines encoding the ancestral D614 S glycoprotein will elicit robust neutralization
217 titers against contemporary G614 isolates, supporting continued development of existing
218 vaccine formulations.

219

220 **Acknowledgements**

221 This work was supported by grants from the U.S. National Institutes of Health, including R01-
222 AI110700, U54-CA260543, U01-AI151797, and R01-AI069274 along with contracts
223 HHSN272201700036I and HHSN272201400008C. This work was supported in part by the
224 Japan Agency for Medical Research and Development under grant numbers JP19fk0108113,
225 JP19fm0108006, JP20fk0108104 and JP19fk0108110. This project was also supported by the
226 North Carolina Policy Collaboratory at the University of North Carolina at Chapel Hill with
227 funding from the North Carolina Coronavirus Relief Fund established and appropriated by the
228 North Carolina General Assembly. We thank Ms. Yuko Sato at the National Institute of
229 Infectious Diseases for technical support with pathological analysis. We are grateful to Adimab
230 LLC. for providing us SARS-CoV-2 nAbs S309, REGN10933, REGN10987 and JS016. We
231 thank Kenichi Okuda and Takafumi Kato at UNC Marsico Lung Institute for technical support on
232 primary cells.

233

234 **References**

235 1. D. Wichmann, J.-P. Sperhake, M. Lütgehetmann, S. Steurer, C. Edler, A. Heinemann, F.
236 Heinrich, H. Mushumba, I. Kniep, A. S. Schröder, C. Burdelski, G. de Heer, A. Nierhaus, D.
237 Frings, S. Pfefferle, H. Becker, H. Bredereke-Wiedling, A. de Weerth, H.-R. Paschen, S.
238 Sheikhzadeh-Eggers, A. Stang, S. Schmiedel, C. Bokemeyer, M. M. Addo, M.

239 Aepfelbacher, K. Püschel, S. Kluge, Autopsy Findings and Venous Thromboembolism in
240 Patients With COVID-19. *Annals of Internal Medicine*. **173**, 268–277 (2020).

241 2. E. W. Cheung, P. Zachariah, M. Gorelik, A. Boneparth, S. G. Kernie, J. S. Orange, J. D.
242 Milner, Multisystem Inflammatory Syndrome Related to COVID-19 in Previously Healthy
243 Children and Adolescents in New York City. *JAMA*. **324**, 294–296 (2020).

244 3. R. Mao, J. Liang, J. Shen, S. Ghosh, L.-R. Zhu, H. Yang, K.-C. Wu, M.-H. Chen,
245 Implications of COVID-19 for patients with pre-existing digestive diseases. *The Lancet
246 Gastroenterology & Hepatology*. **5**, 425–427 (2020).

247 4. Y. J. Hou, K. Okuda, C. E. Edwards, D. R. Martinez, T. Asakura, K. H. Dinnon, T. Kato, R.
248 E. Lee, B. L. Yount, T. M. Mascenik, G. Chen, K. N. Olivier, A. Ghio, L. V. Tse, S. R. Leist,
249 L. E. Gralinski, A. Schäfer, H. Dang, R. Gilmore, S. Nakano, L. Sun, M. L. Fulcher, A.
250 Livraghi-Butrico, N. I. Nicely, M. Cameron, C. Cameron, D. J. Kelvin, A. de Silva, D. M.
251 Margolis, A. Markmann, L. Bartelt, R. Zumwalt, F. J. Martinez, S. P. Salvatore, A. Borczuk,
252 P. R. Tata, V. Sontake, A. Kimple, I. Jaspers, W. K. O'Neal, S. H. Randell, R. C. Boucher,
253 R. S. Baric, SARS-CoV-2 Reverse Genetics Reveals a Variable Infection Gradient in the
254 Respiratory Tract. *Cell*. **182**, 429-446.e14 (2020).

255 5. B. Korber, W. M. Fischer, S. Gnanakaran, H. Yoon, J. Theiler, W. Abfaltrerer, N.
256 Hengartner, E. E. Giorgi, T. Bhattacharya, B. Foley, K. M. Hastie, M. D. Parker, D. G.
257 Partridge, C. M. Evans, T. M. Freeman, T. I. de Silva, A. Angyal, R. L. Brown, L. Carrilero,
258 L. R. Green, D. C. Groves, K. J. Johnson, A. J. Keeley, B. B. Lindsey, P. J. Parsons, M.
259 Raza, S. Rowland-Jones, N. Smith, R. M. Tucker, D. Wang, M. D. Wyles, C. McDanal, L.
260 G. Perez, H. Tang, A. Moon-Walker, S. P. Whelan, C. C. LaBranche, E. O. Saphire, D. C.
261 Montefiori, Tracking Changes in SARS-CoV-2 Spike: Evidence that D614G Increases
262 Infectivity of the COVID-19 Virus. *Cell*. **182**, 812-827.e19 (2020).

263 6. Q. Li, J. Wu, J. Nie, L. Zhang, H. Hao, S. Liu, C. Zhao, Q. Zhang, H. Liu, L. Nie, H. Qin, M.
264 Wang, Q. Lu, X. Li, Q. Sun, J. Liu, L. Zhang, X. Li, W. Huang, Y. Wang, The Impact of
265 Mutations in SARS-CoV-2 Spike on Viral Infectivity and Antigenicity. *Cell*. **182**, 1284-
266 1294.e9 (2020).

267 7. M. R. Denison, R. L. Graham, E. F. Donaldson, L. D. Eckerle, R. S. Baric, Coronaviruses.
268 *RNA Biology*. **8**, 270–279 (2011).

269 8. R. L. Graham, M. M. Becker, L. D. Eckerle, M. Bolles, M. R. Denison, R. S. Baric, A live,
270 impaired-fidelity coronavirus vaccine protects in an aged, immunocompromised mouse
271 model of lethal disease. *Nat Med*. **18**, 1820–6 (2012).

272 9. R. Lorenzo-Redondo, H. H. Nam, S. C. Roberts, L. M. Simons, L. J. Jennings, C. Qi, C. J.
273 Achenbach, A. R. Hauser, M. G. Ison, J. F. Hultquist, E. A. Ozer, *medRxiv*, in press,
274 doi:10.1101/2020.05.19.20107144.

275 10. D. Weissman, M.-G. Alameh, C. C. LaBranche, R. J. Edwards, L. Sutherland, S. Santra, K.
276 Mansouri, S. Gobeil, C. McDanal, N. Pardi, P. A. Shaw, M. G. Lewis, C. Boesler, U. Sahin,
277 P. Acharya, B. F. Haynes, B. Korber, D. C. Montefiori, *medRxiv*, in press,
278 doi:10.1101/2020.07.22.20159905.

279 11. I. O. Omotuyi, O. Nash, O. B. Ajiboye, C. G. Iwegbulam, E. B. Oyinloye, O. A. Oyedele, Z.
280 A. Kashim, K. Okaiyeto, Atomistic simulation reveals structural mechanisms underlying
281 D614G spike glycoprotein-enhanced fitness in SARS-CoV-2. *Journal of Computational
282 Chemistry*. **41**, 2158–2161 (2020).

283 12. R. A. Mansbach, S. Chakraborty, K. Nguyen, D. C. Montefiori, B. Korber, S. Gnanakaran,
284 *bioRxiv*, in press, doi:10.1101/2020.07.26.219741.

285 13. M. Imai, K. Iwatsuki-Horimoto, M. Hatta, S. Loeber, P. J. Halfmann, N. Nakajima, T.
286 Watanabe, M. Ujie, K. Takahashi, M. Ito, S. Yamada, S. Fan, S. Chiba, M. Kuroda, L.
287 Guan, K. Takada, T. Armbrust, A. Balogh, Y. Furusawa, M. Okuda, H. Ueki, A. Yasuhara,
288 Y. Sakai-Tagawa, T. J. S. Lopes, M. Kiso, S. Yamayoshi, N. Kinoshita, N. Ohmagari, S.
289 Hattori, M. Takeda, H. Mitsuya, F. Krammer, T. Suzuki, Y. Kawaoka, Syrian hamsters as a
290 small animal model for SARS-CoV-2 infection and countermeasure development. *PNAS*.
291 **117**, 16587–16595 (2020).

292 14. K. H. Dinnon, S. R. Leist, A. Schäfer, C. E. Edwards, D. R. Martinez, S. A. Montgomery, A.
293 West, B. L. Yount, Y. J. Hou, L. E. Adams, K. L. Gully, A. J. Brown, E. Huang, M. D. Bryant,
294 I. C. Choong, J. S. Glenn, L. E. Gralinski, T. P. Sheahan, R. S. Baric, A mouse-adapted
295 model of SARS-CoV-2 to test COVID-19 countermeasures. *Nature*, 1–9 (2020).

296 15. L. Zhang, C. B. Jackson, H. Mou, A. Ojha, E. S. Rangarajan, T. Izard, M. Farzan, H. Choe,
297 *bioRxiv*, in press, doi:10.1101/2020.06.12.148726.

298 16. M. Imai, T. Watanabe, M. Hatta, S. C. Das, M. Ozawa, K. Shinya, G. Zhong, A. Hanson, H.
299 Katsura, S. Watanabe, C. Li, E. Kawakami, S. Yamada, M. Kiso, Y. Suzuki, E. A. Maher, G.
300 Neumann, Y. Kawaoka, Experimental adaptation of an influenza H5 HA confers respiratory
301 droplet transmission to a reassortant H5 HA/H1N1 virus in ferrets. *Nature*. **486**, 420–428
302 (2012).

303 17. R. A. Urbanowicz, C. P. McClure, A. Sakuntabhai, A. A. Sall, G. Kobinger, M. A. Müller, E.
304 C. Holmes, F. A. Rey, E. Simon-Loriere, J. K. Ball, Human Adaptation of Ebola Virus
305 during the West African Outbreak. *Cell*. **167**, 1079–1087.e5 (2016).

306 18. K. A. Tsetsarkin, S. C. Weaver, Sequential Adaptive Mutations Enhance Efficient Vector
307 Switching by Chikungunya Virus and Its Epidemic Emergence. *PLOS Pathogens*. **7**,
308 e1002412 (2011).

309 19. T. C. S. M. E. Consortium, Molecular Evolution of the SARS Coronavirus During the
310 Course of the SARS Epidemic in China. *Science*. **303**, 1666–1669 (2004).

311 20. J. ter Meulen, E. N. van den Brink, L. L. M. Poon, W. E. Marissen, C. S. W. Leung, F. Cox,
312 C. Y. Cheung, A. Q. Bakker, J. A. Bogaards, E. van Deventer, W. Preiser, H. W. Doerr, V.
313 T. Chow, J. de Kruif, J. S. M. Peiris, J. Goudsmit, Human Monoclonal Antibody
314 Combination against SARS Coronavirus: Synergy and Coverage of Escape Mutants.
315 *PLOS Medicine*. **3**, e237 (2006).

316 21. B. Rockx, D. Corti, E. Donaldson, T. Sheahan, K. Stadler, A. Lanzavecchia, R. Baric,
317 Structural Basis for Potent Cross-Neutralizing Human Monoclonal Antibody Protection
318 against Lethal Human and Zoonotic Severe Acute Respiratory Syndrome Coronavirus
319 Challenge. *J Virol*. **82**, 3220–3235 (2008).

320 22. B. Rockx, T. Sheahan, E. Donaldson, J. Harkema, A. Sims, M. Heise, R. Pickles, M.
321 Cameron, D. Kelvin, R. Baric, Synthetic Reconstruction of Zoonotic and Early Human
322 Severe Acute Respiratory Syndrome Coronavirus Isolates That Produce Fatal Disease in
323 Aged Mice. *Journal of Virology*. **81**, 7410–7423 (2007).

324 23. M. Richard, J. M. A. van den Brand, T. M. Bestebroer, P. Lexmond, D. de Meulder, R. A. M.
325 Fouchier, A. C. Lowen, S. Herfst, Influenza A viruses are transmitted via the air from the
326 nasal respiratory epithelium of ferrets. *Nature Communications*. **11**, 1–11 (2020).

327 24. B. Rockx, T. Kuiken, S. Herfst, T. Bestebroer, M. M. Lamers, B. B. O. Munnink, D. de
328 Meulder, G. van Amerongen, J. van den Brand, N. M. A. Okba, D. Schipper, P. van Run, L.
329 Leijten, R. Sikkema, E. Verschoor, B. Verstrepen, W. Bogers, J. Langermans, C. Drosten,
330 M. F. van Vliessingen, R. Fouchier, R. de Swart, M. Koopmans, B. L. Haagmans,
331 Comparative pathogenesis of COVID-19, MERS, and SARS in a nonhuman primate model.
332 *Science*. **368**, 1012–1015 (2020).

333 25. W. Sungnak, N. Huang, C. Bécavin, M. Berg, R. Queen, M. Litvinukova, C. Talavera-López,
334 H. Maatz, D. Reichart, F. Sampaziotis, K. B. Worlock, M. Yoshida, J. L. Barnes, SARS-
335 CoV-2 entry factors are highly expressed in nasal epithelial cells together with innate
336 immune genes. *Nature Medicine*. **26**, 681–687 (2020).

337 26. A. O. Hassan, N. M. Kafai, I. P. Dmitriev, J. M. Fox, B. K. Smith, I. B. Harvey, R. E. Chen,
338 E. S. Winkler, A. W. Wessel, J. B. Case, E. Kashentseva, B. T. McCune, A. L. Bailey, H.
339 Zhao, L. A. VanBlargan, Y.-N. Dai, M. Ma, L. J. Adams, S. Shrihari, J. E. Danis, L. E.
340 Gralinski, Y. J. Hou, A. Schäfer, A. S. Kim, S. P. Keeler, D. Weiskopf, R. S. Baric, M. J.
341 Holtzman, D. H. Fremont, D. T. Curiel, M. S. Diamond, A single-dose intranasal ChAd
342 vaccine protects upper and lower respiratory tracts against SARS-CoV-2. *Cell* (2020),
343 doi:10.1016/j.cell.2020.08.026.

344 27. Y. Wu, F. Wang, C. Shen, W. Peng, D. Li, C. Zhao, Z. Li, S. Li, Y. Bi, Y. Yang, Y. Gong, H.
345 Xiao, Z. Fan, S. Tan, G. Wu, W. Tan, X. Lu, C. Fan, Q. Wang, Y. Liu, C. Zhang, J. Qi, G. F.
346 Gao, F. Gao, L. Liu, A noncompeting pair of human neutralizing antibodies block COVID-
347 19 virus binding to its receptor ACE2. *Science*. **368**, 1274–1278 (2020).

348 28. J. Hansen, A. Baum, K. E. Pascal, V. Russo, S. Giordano, E. Wloga, B. O. Fulton, Y. Yan,
349 K. Koon, K. Patel, K. M. Chung, A. Hermann, E. Ullman, J. Cruz, A. Rafique, T. Huang, J.
350 Fairhurst, C. Libertiny, M. Malbec, W. Lee, R. Welsh, G. Farr, S. Pennington, D.
351 Deshpande, J. Cheng, A. Watty, P. Bouffard, R. Babb, N. Levenkova, C. Chen, B. Zhang,
352 A. R. Hernandez, K. Saotome, Y. Zhou, M. Franklin, S. Sivapalasingam, D. C. Lye, S.
353 Weston, J. Logue, R. Haupt, M. Frieman, G. Chen, W. Olson, A. J. Murphy, N. Stahl, G. D.
354 Yancopoulos, C. A. Kyratsous, Studies in humanized mice and convalescent humans yield
355 a SARS-CoV-2 antibody cocktail. *Science*. **369**, 1010–1014 (2020).

356 29. D. Pinto, Y.-J. Park, M. Beltramello, A. C. Walls, M. A. Tortorici, S. Bianchi, S. Jaconi, K.
357 Culap, F. Zatta, A. De Marco, A. Peter, B. Guarino, R. Spreafico, E. Cameroni, J. B. Case,
358 R. E. Chen, C. Havenar-Daughton, G. Snell, A. Telenti, H. W. Virgin, A. Lanzavecchia, M.
359 S. Diamond, K. Fink, D. Veesler, D. Corti, Cross-neutralization of SARS-CoV-2 by a
360 human monoclonal SARS-CoV antibody. *Nature*. **583**, 290–295 (2020).

361 30. M. L. Fulcher, S. H. Randell, in *Epithelial Cell Culture Protocols: Second Edition*, S. H.
362 Randell, M. L. Fulcher, Eds. (Humana Press, Totowa, NJ, 2013;
363 https://doi.org/10.1007/978-1-62703-125-7_8), *Methods in Molecular Biology*, pp. 109–121.

364

365 **Material and Method**

366 **Antibodies**

367 Monoclonal SARS-CoV-2 RBD-binding neutralizing antibodies (nAb) B38 and H4 were
368 synthesized at UNC Protein Expression and Purification core based on previously reported
369 protein sequences (27). The nAbs S309, REGN10933, REGN10987 and JS016 were reported
370 previously (28, 29) and were kindly provided by Adimab LLC. Serum samples collected from
371 BALB/c mice vaccinated with WA1 spike protein (D-form) were generated in our laboratory
372 previously (4, 14). Monoclonal antibody targeting the cytoplasmic tail of SARS-CoV-2 S protein
373 was purchased from Abcam (ab272504). Polyclonal antibodies targeting the SARS-CoV N
374 protein PA1-41098 and ANT-180 were purchased from Invitrogen and Prospec, respectively.
375 Mouse antiserum targeting SARS-CoV-2 nucleocapsid protein was produced in our laboratory
376 as described previously (14).

377

378 **Cells and viruses**

379 Simian kidney cell lines Vero-81 (ATCC # CCL81), Vero-E6 (ATCC # CRL1586) were
380 maintained in Eagle's Minimum Essential Medium (Gibco) supplemented with 10% fetal calf
381 serum (FBS, Hyclone). Huh7 and A549-ACE2 cells were maintained in Dulbecco's Modified
382 Eagle Medium (Gibco) with 10% FBS. A clonal A549-ACE2 stable cell line was generated by
383 overexpressing human ACE2 in the A549 cell line (ATCC # CCL185) using the Sleeping Beauty
384 Transposon system. Generation of primary human pulmonary cell cultures was described
385 previously (4). Primary human nasal epithelial cells (HNE) were collected from healthy
386 volunteers by curettage under UNC Biomedical IRB-approved protocols (#11-1363 and #98-
387 1015). Human bronchial epithelial [large airway epithelial (LAE)] and bronchiolar [small airway

388 epithelial (SAE)] cells were isolated from freshly excised normal human lungs obtained from
389 transplant donors with lungs unsuitable for transplant under IRB-approved protocol (#03-1396)
390 and cultured in air liquid interface (ALI) media, as previously described (4, 30). SARS-CoV-2
391 WA1 molecular clone, WT and nLuc viruses were generated previously (4, 14). To generate the
392 D614G and D614G-nLuc variants, the amino acid substitution was introduced into the S gene in
393 the plasmid F and coupled with plasmid G with or without nLuc insertion in the ORF7a. Then,
394 the seven genomic cDNA fragments spanning the entire SARS-CoV-2 genome were digested,
395 purified and ligated. Full-length RNA was transcribed and electroporated into Vero E6 cells.
396 Virus stocks were verified by Sanger sequencing. All viral infections were performed under
397 biosafety level 3 (BSL-3) conditions at negative pressure, and Tyvek suits connected with
398 personal powered-air purifying respirators.

399

400 **nLuc virus entry assay**

401 Monolayers of Vero-E6, Vero-81, A549-ACE2 and Huh7 cells were cultured in black-walled 96-
402 well plates (Corning 3904) overnight. The cells were infected with WT-nLuc or D614G-nLuc
403 viruses at MOI of 0.1. After incubation for 1h, inocula were removed, and the cells were washed
404 two times with PBS and maintained in DMEM containing 5% FBS and the mixture of SARS-
405 CoV-2 nAbs REGN10933, REGN10987 and JS016 at concentration of 1000 times of IC₅₀ for
406 each. After incubation at 37°C for 48h, viral infection was quantified using nLuc activity via Nano-
407 Glo Luciferase Assay System (Promega) according to the manufacturer specifications.

408

409 **SARS-CoV-2 neutralization assay**

410 Vero E6 cells were plated at 20,000 cells per well in black-walled 96-well plates (Corning 3904).
411 Mouse serum samples were tested at a starting dilution of 1:20 and mAb samples were tested
412 at a starting dilution 30 to 0.1 µg/ml and were serially diluted 3-fold up to eight dilution spots.
413 Diluted antibodies or sera were mixed with 189 PFU/well WT-nLuc or D614G-nLuc virus, and

414 the mixtures were incubated at 37°C for 1 hour. Following incubation, growth media was
415 removed, and virus-antibody mixtures were added to the cells in duplicate. Virus-only controls
416 were included in each plate. Following infection, plates were incubated at 37°C with 5% CO₂ for
417 48h. After the 48h incubation, cells were lysed, and luciferase activity was measured via Nano-
418 Glo Luciferase Assay System (Promega) according to the manufacturer specifications.
419 Neutralization titers were defined as the sample dilution at which a 50% reduction in relatively
420 light unit (RLU) was observed relative to the average of the virus control wells.

421

422 **WT and D614G competition assay and BstCI digestion**

423 LAE cultures from one donor were infected with MOI of 0.5 of WT and D614G mixture at 1:1
424 and 10:1 ratios. Following 1h incubation, the cultures were washed three times with PBS and
425 cultures for 72h in the air-liquid interface (ALI) condition. To passage the progeny viruses,
426 100uL PBS was added to each LAE surface for 10 min incubation and was added to naïve
427 cultures surface for infection. The virus samples were continuously passaged three times in LAE
428 culture, and cellular RNA samples from the 3rd passage were extracted using TRIzol reagent
429 (Thermo Fisher). A 1547bp fragment containing the D614G site was amplified from each RNA
430 samples by RT-PCR using primer set: 5'-GTAATTAGAGGTGATGAAGTCAGAC-3' and 5'-
431 GAACATTCTGTGTAACTCCAATACC-3'. The amplicon was purified by agarose gel
432 electrophoresis and digested with BstCI restriction enzyme (NEB) overnight. The digested
433 products were analyzed on agarose gel electrophoresis.

434

435 **hACE2 mice infection and titration**

436 Mouse study was performed in accordance with Animal Care and Use Committee guidelines of
437 the University of North Carolina at Chapel Hill. *HFH4-hACE2* transgenic mice were bred and
438 maintained at UNC. Mice were infected with 10⁵ PFU of WT or D614G viruses intranasally

439 under ketamine/xylazine anesthesia. At indicated timepoints, a subset of mice were euthanized
440 by isoflurane overdose, and tissue samples were harvested for viral titer analysis. The right
441 caudal lung lobe, brain and nasal turbinates were taken for titer and stored at -80 °C until
442 homogenized in 1mL PBS and titrated by plaque assay. Briefly, the supernatants of
443 homogenized tissue were serially diluted in PBS, 200 μ L of diluted samples were added to
444 monolayers of Vero-E6 cells, followed by agarose overlay. Plaques were visualized by day 2
445 post staining with neutral red dye.

446

447 **Whole-mount immunostaining and imaging**

448 WT or D614G-infected LAE ALI cultures were fixed twice for 20 minutes in 4% formaldehyde in
449 PBS and stored in PBS. The SARS-CoV-2 N antigen was stained with polyclonal rabbit anti-
450 SARS-CoV N protein (Invitrogen PA1-41098, 0.5 ug/mL), and using species-specific secondary
451 antibodies as previously described (4). The cultures were also imaged for α -tubulin (Millipore
452 MAB1864; 3ug/mL) and MUC5AC (Thermo Scientific 45M1; 4ug/mL) as indicated. Filamentous
453 actin was localized with phalloidin (Invitrogen A22287), and nuclei was visualized with Hoechst
454 33342 staining (Invitrogen). An Olympus FV3000RS confocal microscope in Galvo scan mode
455 was used to acquire 5-channel Z stacks by 2-phase sequential scan. Representative stacks
456 were acquired and are shown as Z-projections and XZ cross sections to distinguish individual
457 cell features and to characterize the infected cell types. ImageJ was used to measure the
458 relative apical culture surface covered by multiciliated cells.

459

460 **Western blot analysis of spike protein cleavage**

461 Exocellular SARS-CoV-2 virions were collected from WT or D614G infected LAE culture by
462 gently washing intact apical surface with 100uL PBS. Samples from the triplicated cultures were
463 pooled, lysed with modified RIPA buffer and inactivated at 98 °C. Protein samples were
464 electrophoresed in 4-20% continuous SDS-PAGE gel (Bio-Rad) and transferred on to a PVDF

465 membrane (Bio-Rad). SARS-CoV-2 S protein was probed using a mAb targeting SARS-CoV-2
466 S mAb (Abcam, ab272504) and the N protein was probed using a mouse antiserum produced in
467 our laboratory. The N protein was used as a loading control for the Western blot.

468

469 **EM imaging and Spike quantification**

470 WT or D614G infected primary cell cultures were submerged in fixative (4% paraformaldehyde,
471 2.5% glutaraldehyde and 0.1 M sodium cacodylate) overnight. For SEM, samples were rinsed,
472 fixed with 1% OsO₄ (Electron Microscopy Sciences) in perfluorocarbone FC-72 (Thermo
473 Fischer) solution for 1 hour. After dehydration and mounted on aluminum planchets, samples
474 were imaged using a Supra 25 field emission scanning electron microscope (Carl Zeiss
475 Microscopy). For TEM, fixed samples were rinsed and post-fixed with potassium-ferrocyanide
476 reduced osmium (1% osmium tetroxide/1.25% potassium ferrocyanide/0.1 sodium cacodylate
477 buffer. The cells were dehydrated and embedment in Polybed 812 epoxy resin (Polysciences).
478 The cells were sectioned perpendicular to the substrate at 70nm using a diamond knife and
479 Leica UCT ultramicrotome. Ultrathin sections were collected on 200 mesh copper grids and
480 stained with 4% aqueous uranyl acetate followed by Reynolds' lead citrate. Samples were
481 observed using a JEM-1230 transmission electron microscope operating at 80kV and images
482 were taken using a Gatan Orius SC1000 CCD camera (Gatan). The number of spikes on each
483 virion projection was quantified using ImageJ software. SEM images of infected cultures from 3
484 donors were imaged, at least 10 different micrographs (>100k X) were analyzed using the multi-
485 point counting tool on individual virions.

486

487 **Hamster infection, tissue collection, and transmission studies**

488 Hamster studies were performed in accordance with Animal Care and Use Committee
489 guidelines of the University of Wisconsin-Madison. Syrian hamsters (females, 4-6 weeks old)
490 were purchased from Envigo (Madison, WI) and allowed to acclimate for a minimal of three days

491 at BSL-3 agriculture containment at the Influenza Research Institute (University of Wisconsin).
492 Hamsters were infected with 10^3 PFU of WT or D614G viruses intranasally under isoflurane
493 anesthesia. At the indicated timepoints, a subset of hamsters were euthanized by deep
494 anesthesia by isoflurane inhalation and cervical dislocation and tissues samples were harvested
495 for virus titer and histopathology analysis. Weights of one group of hamsters were recorded for
496 14 days after infection.

497

498 To evaluate indirect virus transmission between hamsters, groups of hamsters (n=8 per group)
499 were infected with 10^3 PFU of WT or D614G viruses intranasally under isoflurane anesthesia.
500 Infected animals were placed in specially designed cages (Figure S2B) inside an isolator unit
501 (16). Twenty-four hours later, naïve hamsters were placed in the other side of the cage with 5
502 cm separation by a double-layered divider to allow free air flow. The isolator unit provided one
503 directional airflow; therefore, the infected hamsters were placed in the front of the isolator unit.
504 Metal shroud were placed over the cages so only the front and back of the cage was open.
505 Nasal washes were collected at 3-day intervals for the infected hamsters and 2-day intervals for
506 the exposed animals starting on day 2 after infection or exposure (Figure S2A).

507

508 **Pathological examination**

509 Tissues fixed for at least seven days in 10% formalin were trimmed and embedded in paraffin.
510 The paraffin blocks were cut into 3 μ m-thick sections and mounted on silane-coated glass slides.
511 One section from each tissue sample was stained using a standard hematoxylin and eosin
512 procedure. To detect SARS-CoV-2 Nucleocapsid protein in immunohistochemistry (IHC), tissue
513 sections were incubated with a rabbit polyclonal antibody (Prospec, ANT-180) as the primary
514 antibodies, and peroxidase-labeled polymer-conjugated anti-rabbit immunoglobulin
515 (EnVision/HRP, DAKO) as the secondary antibody. Immunostaining was visualized by 3,3'-

516 diaminobenzidine tetrahydrochloride staining. Hematoxylin (Modified Mayer's) was used as a
517 nuclear counterstain for IHC.

518

519 **Figure legends**

520 **Figure 1. SARS-CoV-2 D614G variant demonstrate enhanced infectivity in some cell lines**
521 **and replication fitness in upper respiratory epithelia.** A. Genomes of recombinant SARS-
522 CoV-2 D614G variants. B. Entry efficiency of WT-nLuc and D614G-nLuc in multiple cell lines at
523 MOI of 0.1. After 1h infection, cells were cultured in the medium containing neutralization
524 antibodies to minimize the secondary round of infection. The relative light unit (RLU)
525 representing the nLuc expression level was measured at 8h post infection. C. Multi-step growth
526 curves of the two variants at Vero-E6 (i), Vero-81 (ii) and A549-ACE2 (iii) and Huh7 (iv) cell
527 lines at MOI = 0.5. Comparison of 24, 48 and 72h titers between the two variants infected
528 primary nasal (D), large airway (E) and small airway (F) cells in triplicate. Triplicated titers of the
529 two viruses in the cultures from the same donor were analyzed by paired t-test. G. Schematic of
530 competition assay on large airway epithelial cells. Cultures were infected with 1:1 or 10:1 ratio of
531 WT and D614G mixture at MOI at 0.5, and serially passaged three times. H. BstCI digestion of
532 the partial S gene from the competition assay samples. A 1.5kb fragment containing the residue
533 614 was amplified from the total RNA collected from competition assay. I. Sanger sequencing
534 chromatogram of S RNA collected from the competition assay. Data between the WT and
535 D614G viruses in B and C are analyzed using unpaired t-test, and the data between the two
536 groups in D, E and F are analyzed using paired t-test. N.S., not significantly different, $p > 0.05$;
537 *, $p < 0.05$ **, $p < 0.01$; ***, $p < 0.001$.

538

539 **Figure 2. D614G substitution does not alter SARS-CoV-2 virion morphology and S protein**
540 **cleavage pattern but change viral sensitivity to neutralizing antibodies.** A. Transmission
541 electron microscopy image of WT and D614G virions on airway epithelial cell surface, scale bar:

542 200 nm. B. Scanning electron microscopy images of WT and D614G virions on airway epithelial
543 cell surface, scale bar: 100 nm. C. Quantification of S protein on individual SARS-CoV-2 virion
544 projections. The number of S protein on individual virion projections from different SEM images
545 were quantify manually, n=20. D. Western blot analysis of SARS-CoV-2 virions washed from
546 WT- or D614G-infected LAE culture surface at 72h. Each lane contains mixed sample from
547 triplicated cultures. Full-length (S), S1/S2 cleaved and S2' cleaved spike protein (upper panel)
548 and nucleocapsid protein (lower panel) were probed. E. ID₅₀ values of 10 serum samples
549 collected from D614-form Spike-vaccinated mice neutralizing WT- and D614G-nLuc viruses. F.
550 Three representative neutralization curves of the mouse sera against both viruses. Summarized
551 IC₅₀ values (G) and individual neutralization curves (H) of 6 human nAbs against both viruses.
552 Data between the WT and D614G viruses in E and G are analyzed using paired t-test. N.S., not
553 significantly different, $p > 0.05$; **, $p < 0.01$.

554

555 **Figure 3. D614G variant exhibit similar pathogenesis but faster transmission than the WT**
556 **virus *in vivo*.** A. Lung, brain and nasal turbinate titers of WT and D614G infected hACE2 mice
557 were determined on day 2 (i) day 5 (ii). Each mouse was infected with 10⁵ PFU of the virus, n=
558 5/group, plaque assay detection limit (1.7 log₁₀PFU/mL) is indicated in a dash line. Viral titers of
559 lung (B) and nasal turbinates (C) collected from SARS-CoV-2 infected hamsters at day 3 and 6.
560 Each hamster was infected with 10³ PFU of virus, plaque assay detection limit (1 log₁₀PFU/mL)
561 is indicated in a dash line. D. Body weight of mock-, WT- and D614G-infected hamsters, n =
562 4/group. E. Immunohistochemistry (IHC) staining of SARS-CoV-2 nucleocapsid protein in the
563 representative lung tissues collected from WT- and D614G-infected hamsters, scale bar = 100
564 μ m. F. H&E staining of representative lung tissues collected on day 3, 6, and 9 from hamsters
565 infected with WT or D614G, scale bar : 1mm. G-i: Quantification of IHC positive cells in hamster
566 lung tissues, following scoring system: 0, no positive cell; 1, <10%; 2, 10-50%; 3, >50% of
567 positive cells in each lobe of lung. G-ii. The size of pulmonary lesion was determined based on

568 the mean percentage of affected area in each section of the collected lobes from each animal.
569 G-iii Pathological severity scores in infected hamsters, based on the percentage of inflammation
570 area for each section of the five lobes collected from each animal following scoring system: 0,
571 no pathological change; 1, affected area ($\leq 10\%$); 2, affected area ($<50\%, >10\%$); 3, affected
572 area ($\geq 50\%$); an additional point was added when pulmonary edema and/or alveolar
573 hemorrhage was observed. (H) Viral titers in nasal washes collected from the infected and
574 exposed hamster pairs in WT and D614G groups; plaque assay detection limit ($1 \log_{10}\text{PFU/mL}$)
575 is indicated in a dash line. Data between the WT and D614G viruses in A, B, C, D, and G are
576 analyzed using unpaired t-test. The number of transmitted hamsters at different timepoints are
577 analyzed by Fisher exact test. N.S., not significantly different, $p > 0.05$.

578

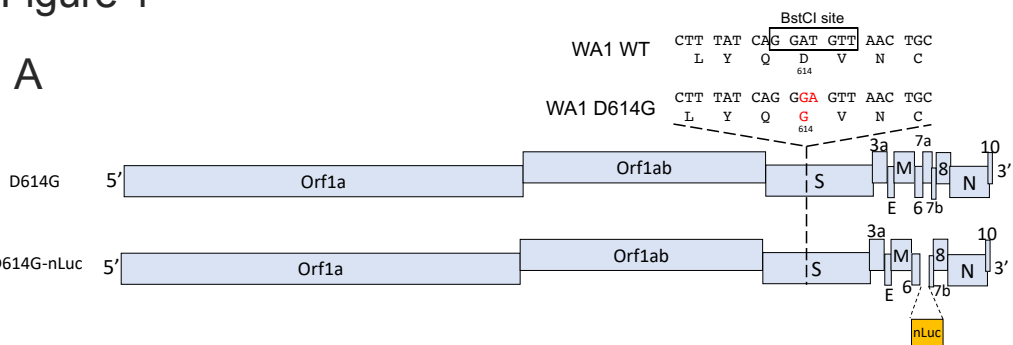
579 **Figure S1. Additional data of WT and D614G infected primary human airway epithelial**
580 **cells.** A. Growth curves of the two viruses in individual primary nasal (i), large airway (ii) and
581 small airway (iii) epithelial cells relating to Fig 1 D to F, MOI = 0.1; plaque assay detection limit:
582 $1.7 \log_{10}\text{PFU/mL}$. B. comparison of WT and D614G titer at 96h on HNE, LAE and SAE. C.
583 Whole-mount staining of WT and D614G infected LAE cultures, blue: Hoechst (nuclei), red:
584 phalloidin (F-actin), white: cilia (α -tubulin); yellow: MUC5AC, Green: SARS-CoV-2 N protein,
585 scale bar: 50 μm .

586

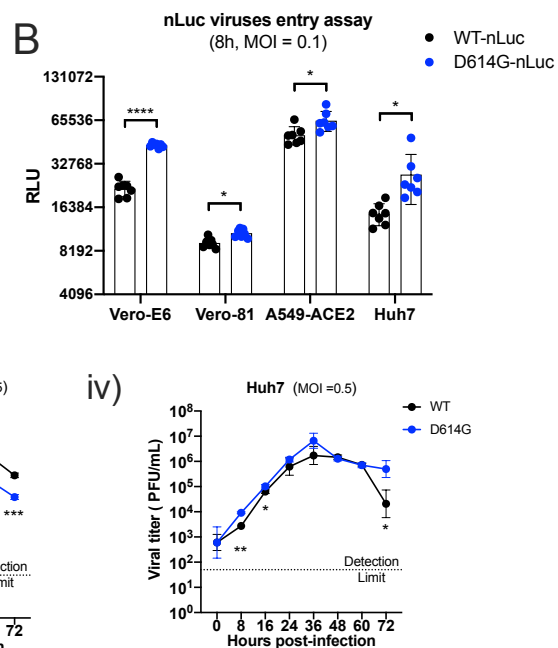
587 **Figure S2. Experimental design of hamster transmission study.** A, Timeline of nasal wash
588 sampling from infected and exposed animals. B. Image of hamsters in the cage in transmission
589 study.

Figure 1

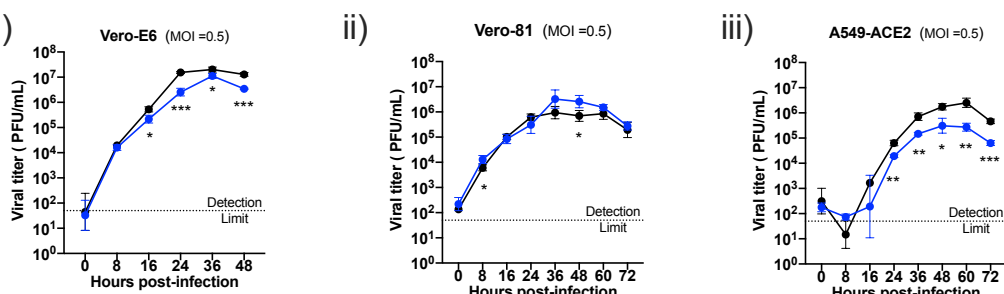
A



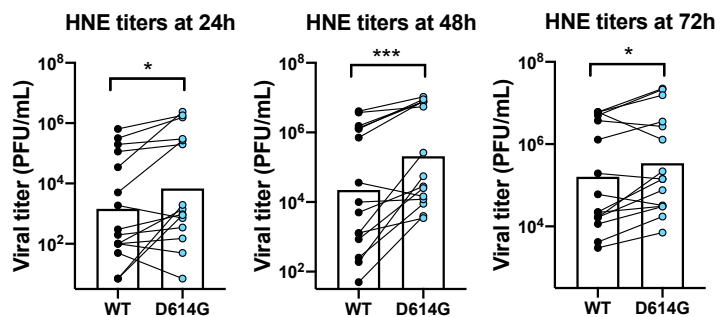
B



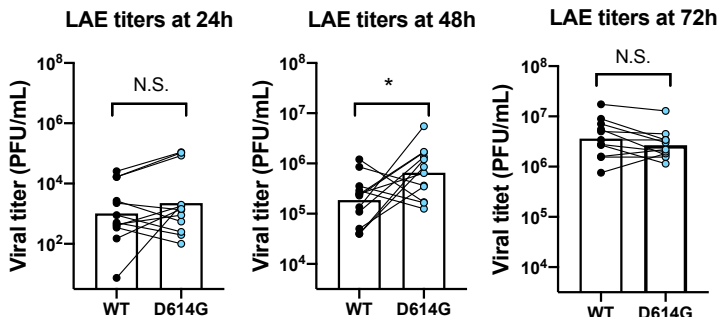
C



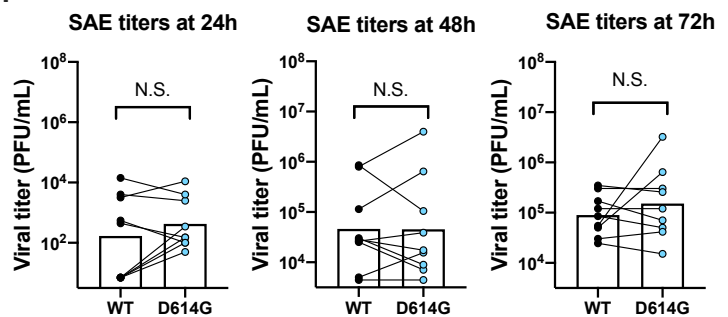
D



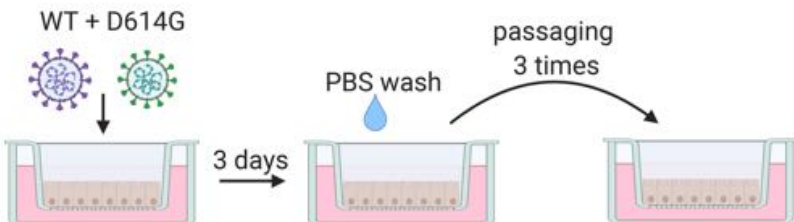
E



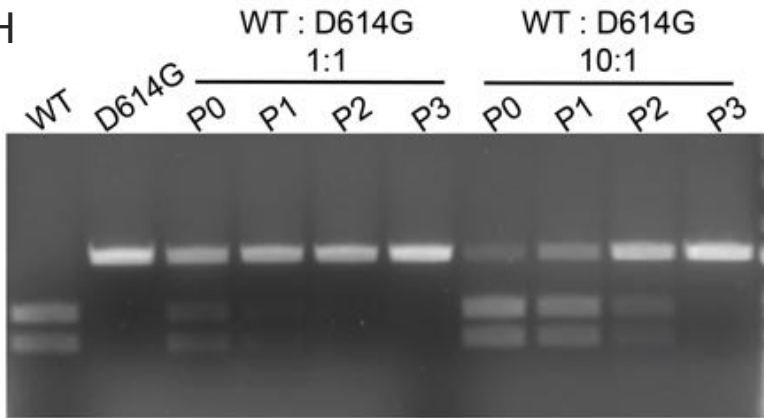
F



G



H



I

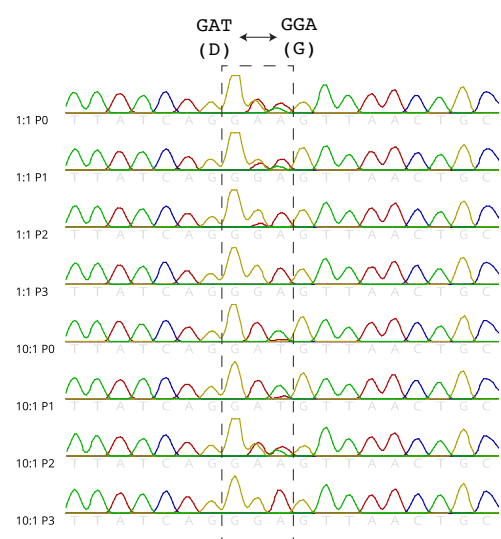


Figure 2

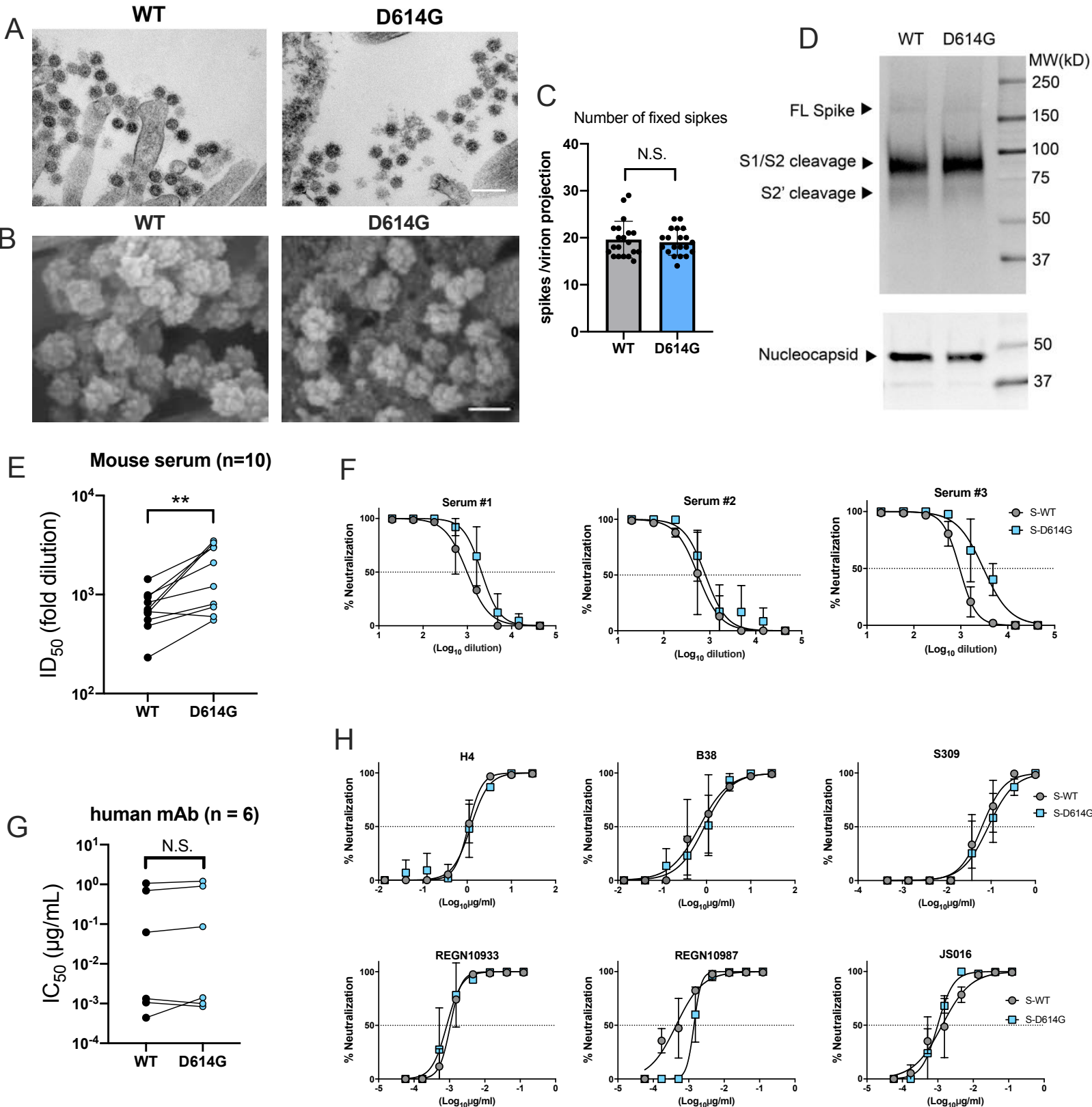
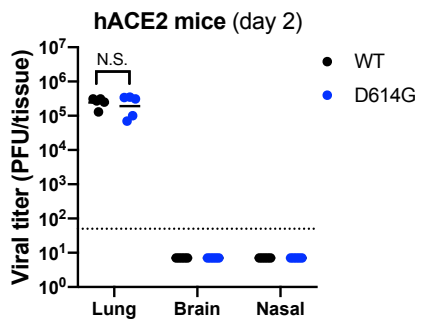
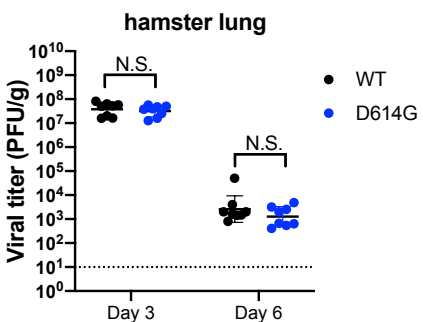


Figure 3

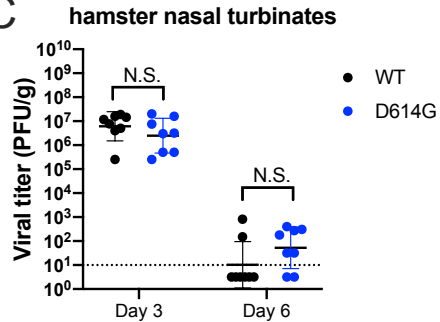
A i)



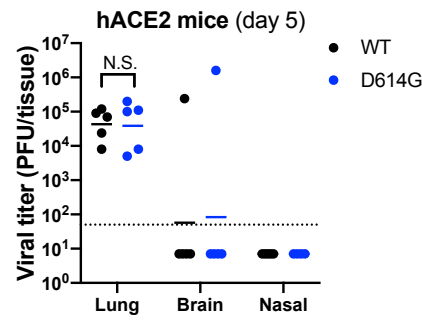
B



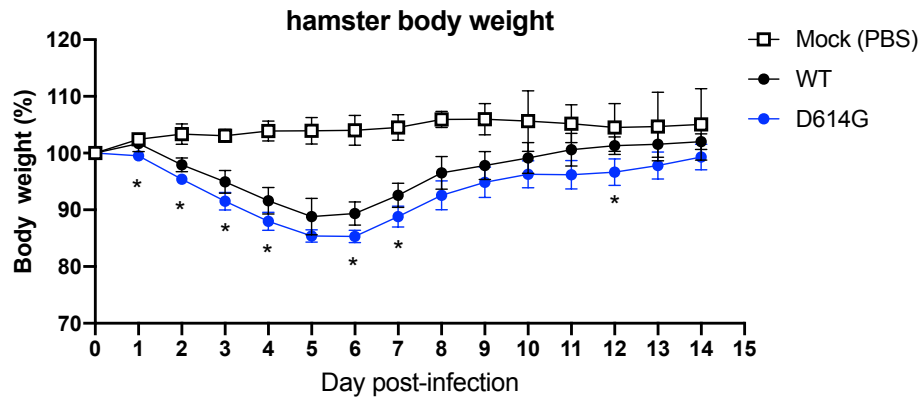
C



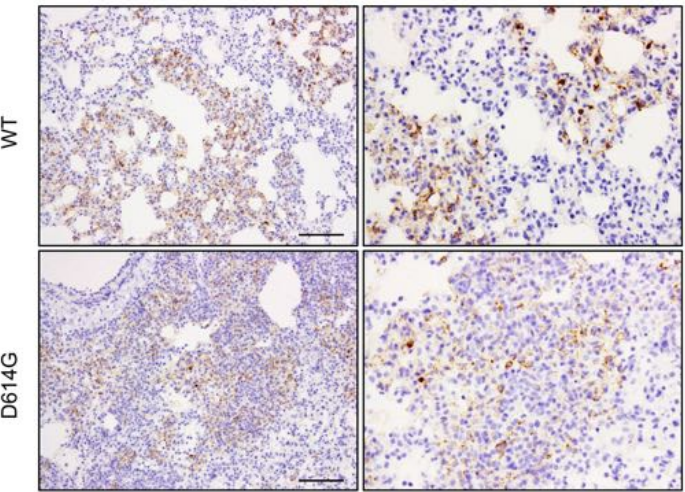
ii)



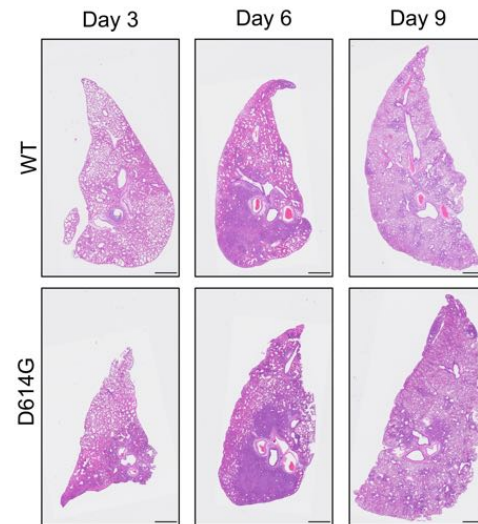
D



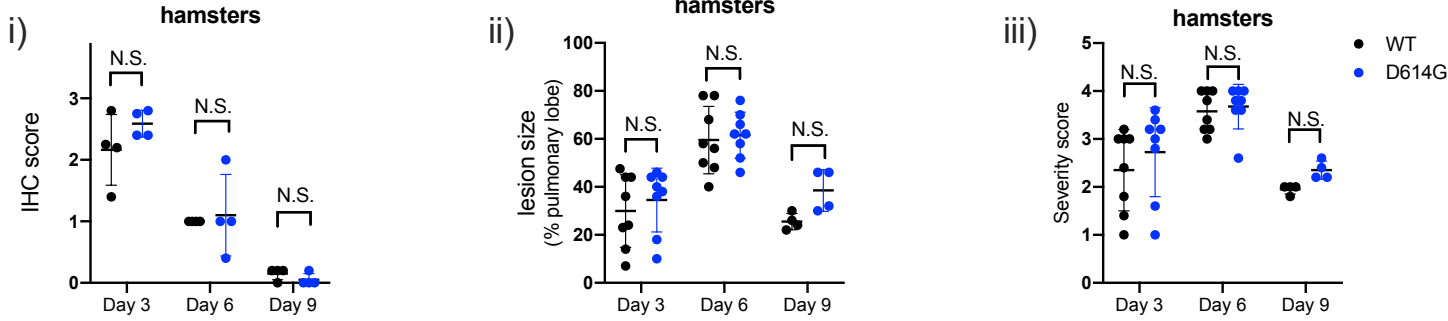
E



F



G



H

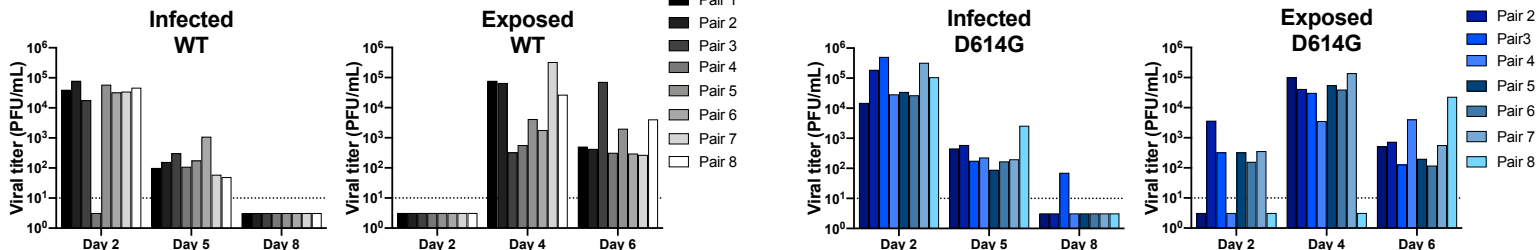
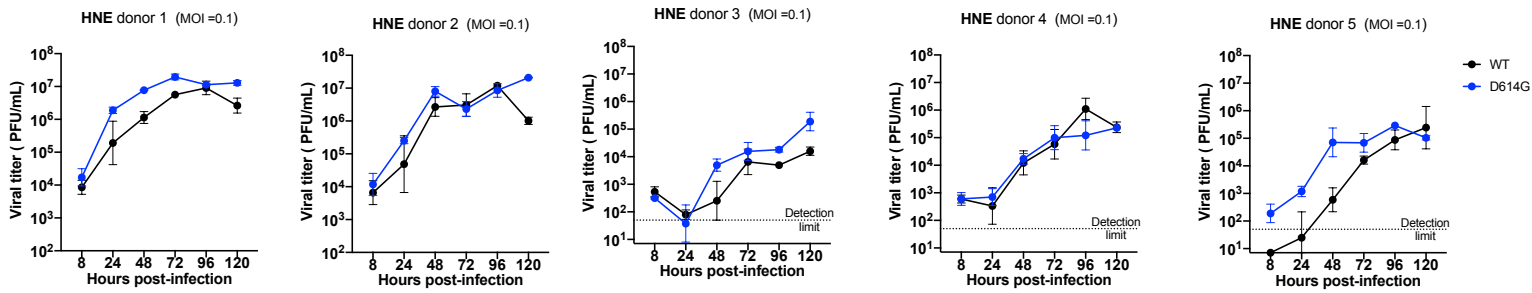


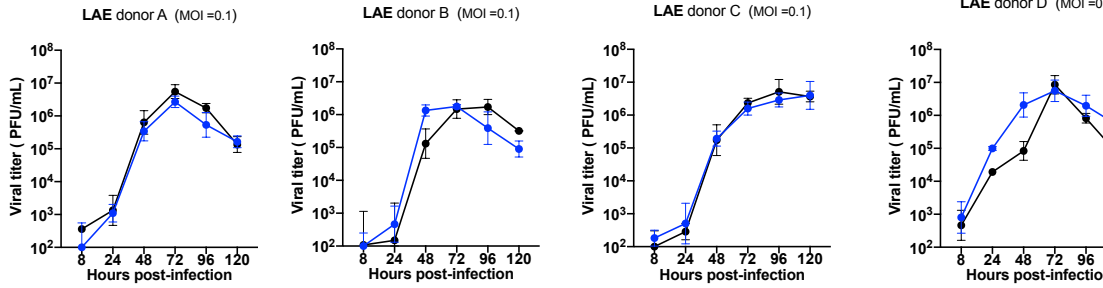
Figure S1

A

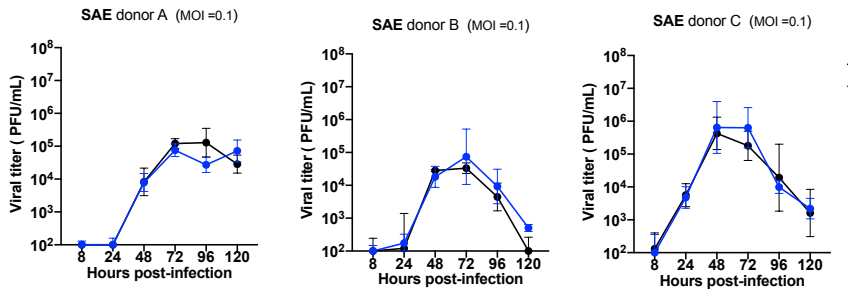
i)



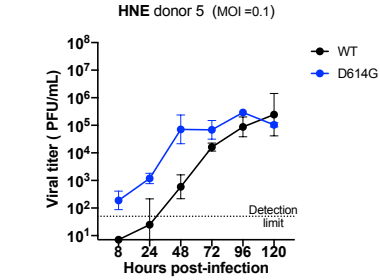
ii)



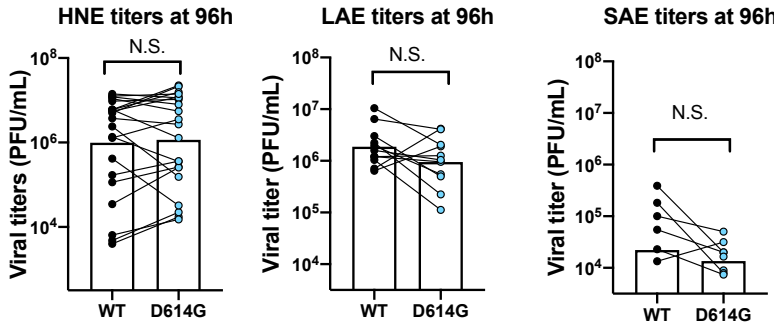
iii)



LAE donor D (MOI = 0.1)



B



C

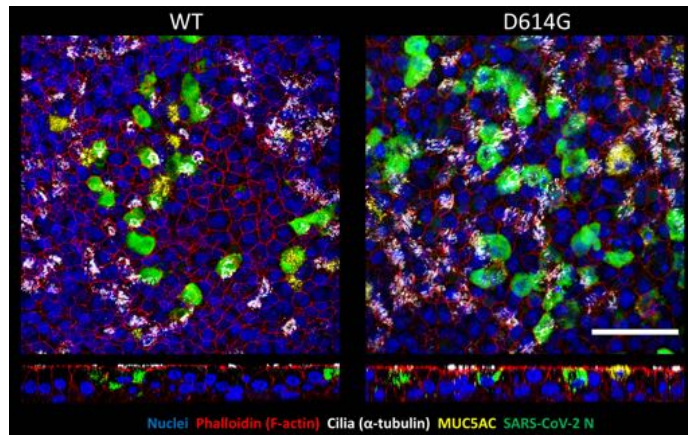


Figure S2

A

| | | | | | | | | | |
|--|---|---|---|---|---|---|---|---|---|
| Infected hamsters (Day post infection) | 0 | 1 | 2 | 3 | 4 | 5 | 6 | 7 | 8 |
| Exposed hamsters (Day post exposure) | - | 0 | 1 | 2 | 3 | 4 | 5 | 6 | 7 |

 : nasal wash sampling

 : nasal wash sampling

B

